Evolution of structural and electronic properties of highly mismatched InSb films

X. Weng and R. S. Goldman[a)]
Department of Materials Science and Engineering, University of Michigan, Ann Arbor, Michigan 48109-2136

D. L. Partin and J. P. Heremans
Delphi Research and Development Center, Warren, Michigan 48090-9055

(Received 15 June 2000; accepted for publication 18 September 2000)

We have investigated the evolution of structural and electronic properties of highly mismatched InSb films, with thicknesses ranging from 0.1 to 1.5 μm. Atomic force microscopy, cross-sectional transmission electron microscopy, and high-resolution x-ray diffraction show that the 0.1 μm films are nearly fully relaxed and consist of partially coalesced islands, which apparently contain threading dislocations at their boundaries. As the film thickness increases beyond 0.2 μm, the island coalescence is complete and the residual strain is reduced. Although the epilayers have relaxed equally in the $\langle 110 \rangle$ in-plane directions, the epilayer rotation about an in-plane axis (epilayer tilt) is not equal in both $\langle 110 \rangle$ in-plane directions. Interestingly, the island-like surface features tend to be preferentially elongated along the axis of epilayer tilt. Furthermore, epilayer tilt which increases the substrate offcut (reverse tilt) is evident in the $[110]$ direction. High-resolution transmission electron microscopy indicates that both pure-edge and 60° misfit dislocations contribute to the relaxation of strain. In addition, as the film thickness increases, the threading dislocation density decreases, while the corresponding room-temperature electron mobility increases. The other structural features, including the residual strain, and the surface and interface roughness, do not appear to impact the electron mobility in these InSb films. Together, these results suggest that free-carrier scattering from the threading dislocations is the primary room-temperature mobility-limiting mechanism in highly mismatched InSb films. Finally, we show *quantitatively* that free-carrier scattering from the lattice dilation associated with threading dislocations, rather than scattering from a depletion potential surrounding the dislocations, is the dominant factor limiting the electron mobility. © *2000 American Institute of Physics.* [S0021-8979(00)08924-6]

I. INTRODUCTION

Due to its small direct band gap (0.17 eV), low effective mass ($0.013m_e$), and high room-temperature electron mobility ($\sim 7\times 10^4$ cm^2/V s), InSb is suitable for many device applications, including long-wavelength infrared sources and magnetoresistive sensors.[1] InSb films are often grown on GaAs substrates, which are electrically insulating and stronger and cheaper than bulk InSb wafers. InSb/GaAs heterostructures have been grown successfully by several techniques, including molecular beam epitaxy (MBE) (Refs. 2–12) and metalorganic chemical vapor deposition (MOCVD).[13–20] Because of the high mismatch ($\sim$14.6%) between the InSb film and the GaAs substrate, InSb films initially grow in the Volmer–Weber mode, which consists of nucleation and coalescence of three-dimensional islands. The island growth may introduce significant surface and interface roughness, which may in turn impact the electron mobility of thin films when the spatial length scale of the roughness is comparable to the Fermi wavelength.[21]

The large mismatch between the InSb film and the GaAs substrate also introduces a high density of strain-relaxation-induced defects, including misfit and threading dislocations. An interfacial network of $(a/2)\langle 110 \rangle$ pure-edge dislocations spaced 32 Å apart has been observed in MBE-grown InSb/GaAs heterostructures.[4,6,8] In other studies, the threading dislocation density has been estimated to be as high as 10^{11}/cm^2 in the region close to the interface.[3,7,22] Dislocations may reduce the electron mobility through Coulomb potential scattering[23–26] and deformation potential scattering.[27] Physically, these two effects correspond to free-carrier scattering either from a depletion potential surrounding the dislocations, or from the lattice dilation associated with the dislocations. In semiconductors without inversion symmetry, e.g., III–V or II–VI compounds, the piezoelectric potential associated with the dislocations also reduces the electron mobility.[28] Previous studies of $>$1-μm-thick InSb films have shown that the maximum electron mobility occurs close to room temperature, and the mobility decreases as the temperature is lowered.[2,5,29] Parker *et al.* found that InSb films with a doping slab at the film/substrate interface had more than a factor of 2 lower mobility for the same carrier concentration than the films where the slab was inserted at $\sim$0.75 μm from the interface.[7] These effects have been attributed to free-carrier scattering from threading dislocations, presumably due to the lattice dilation associated with the dislocations.[27] However, to date, a quantitative consideration

[a)]Electronic mail: rsgold@engin.umich.edu

 © 2000 American Institute of Physics

of the effects of dislocations on the electron mobility of InSb has not been reported. Furthermore, in InSb, the relative effects of free-carrier scattering from the lattice dilation associated with threading dislocations and from a depletion potential surrounding the dislocations have not been considered.

To date, the evolution of the microstructure of MBE-grown InSb has been investigated in detail only for the thinnest (0.35–100 nm) and thickest (0.5–10 μm) films.[3,4,8,22] There have been fewer studies of the structural evolution of MOCVD-grown InSb on GaAs.[19,20] The relative effects of dislocations and surface or interface roughness on the electronic properties of InSb/GaAs heterostructures are not well understood. Furthermore, a complete understanding of the structural and electronic properties of InSb/GaAs heterostructures is essential for the optimization of both electronic and photonic device performance. Therefore, we have examined the evolution of the structure and electronic properties of a series of highly mismatched InSb films grown by metalorganic chemical vapor deposition on GaAs substrates. Using atomic force microscopy (AFM) and cross-sectional transmission electron microscopy (TEM), we find that the 0.1 μm films consist of partially coalesced islands with threading dislocations at their boundaries. As the film thickness is increased beyond 0.2 μm, the islands have apparently finished coalescing. High-resolution x-ray diffraction (HRXRD) shows that the residual strain decreases as the film thickness increases, resulting in epilayers which are nearly fully and symmetrically relaxed in the $\langle 110 \rangle$ in-plane directions. High-resolution TEM indicates that both pure-edge and 60° misfit dislocations contribute to the relaxation of strain. Epilayer rotation about an in-plane axis (epilayer tilt), which is not equal in both $\langle 110 \rangle$ in-plane directions, is observed. In addition, reverse tilt, which increases the substrate offcut, is apparent. The island-like surface features mentioned above tend to preferentially grow in the same direction as that of the epilayer tilt axis. The threading dislocation density decreases as a function of film thickness, dropping from $\sim 10^{11}\ \mathrm{cm}^{-2}$ for the 0.1 μm films to $\sim 4\times 10^{8}\ \mathrm{cm}^{-2}$ for the 1.5 μm films. The reduction in threading dislocation density as a function of film thickness is consistent with a significant increase in room-temperature electron mobility. Furthermore, the room-temperature electron mobility of our bulk-like films is not apparently limited by residual strain, or surface or interface roughness. Together, these results suggest that free-carrier scattering from the threading dislocations is the dominant factor limiting the room-temperature electron mobility in highly mismatched InSb films. We also show *quantitatively* that the dislocation-induced free-carrier scattering is primarily due to the lattice dilation associated with the dislocations rather than the depletion potential surrounding the dislocations.

The article is organized as follows. In Sec. II, we describe the procedures used for the experimental studies, including metalorganic chemical vapor deposition, Hall measurements, cross-sectional and plan-view transmission electron microscopy, high-resolution transmission electron microscopy (HRTEM), atomic-force microscopy, and high-resolution x-ray diffraction measurements. In Sec. III, the evolution of surface morphology, epilayer tilt, strain relaxation, threading dislocations, and electronic properties are presented. The relative effects of the structural factors on the electronic properties and the interplay between the strain relaxation, epilayer tilt, surface morphology, and misfit dislocations are also discussed. Conclusions are given in Sec. IV.

II. EXPERIMENTAL PROCEDURES

InSb films with thicknesses of 0.1, 0.2, 0.55, and 1.5 μm were grown by MOCVD on semi-insulating GaAs(001) substrates, intentionally miscut by 2° towards the $(\bar{1}01)$ plane. Hence, the substrate surface normal is rotated 2° away from the (001), toward the $(\bar{1}01)$ plane, which is about the miscut axis [010]. The samples were grown using an indium nucleation technique which involved exposure to TMIn several seconds before trisdimethyl aminoantimony was switched into the reactor. The details of the growth conditions have been reported elsewhere.[18] In order to identify the in-plane $\langle 110 \rangle$ orientations, the backside of the substrate of each sample was etched with HF/H_2O_2 (1:4).[30]

We examined the surface morphology of the films using a combination of atomic force microscopy and cross-sectional transmission electron microscopy (XTEM). AFM was performed using a Digital Instruments Nanoscope III operating in tapping mode with etched silicon probes. In order to rule out possible tip-shape artifacts, for each sample, we utilized several new probes for imaging a variety of surface regions. We will present images displaying features typical of the sample surface, which are not associated with tip-shape artifacts. For all the AFM images, we applied second-order flattening, in order to remove the tilt and bow in each scan line. The root-mean-square surface roughness (R_{rms}) was determined from the AFM data using

$$R_{\mathrm{rms}}=\left[\frac{1}{N}\sum_{1}^{N}(h_i-\bar{h})^2\right]^{1/2}, \tag{1}$$

where N is the number of data points, h_i are the data points that describe the relative vertical height of the surface, and $\bar{h}$ is the mean height of the surface. Since the R_{rms} value only provides the average surface roughness, we also performed a power spectral density (PSD) analysis to obtain the spatial frequencies of the roughness.[31] The PSD analysis enables us to examine correlations between roughness, specific surface features, and the electronic properties of the films.

For TEM studies, cross-sectional specimens were prepared using conventional mechanical thinning followed by argon-ion milling at 77 K. Plan-view TEM specimens were prepared using mechanical polishing followed by chemical etching from the substrate side. NH_4OH/H_2O_2 (4:1) and $HF/HNO_3/H_2O$ (1:1:4) were used to etch off the GaAs substrate and InSb films, respectively. The cross-sectional and plan-view TEM were carried out on a JEOL 2000FX transmission electron microscope operating at 200 kV. High-resolution TEM was performed using a JEOL 4000EX transmission electron microscope at 400 kV.

High-resolution x-ray diffraction measurements were performed on a Bede D[1] system. For each film, symmetric (004) and asymmetric (115) rocking curves were collected

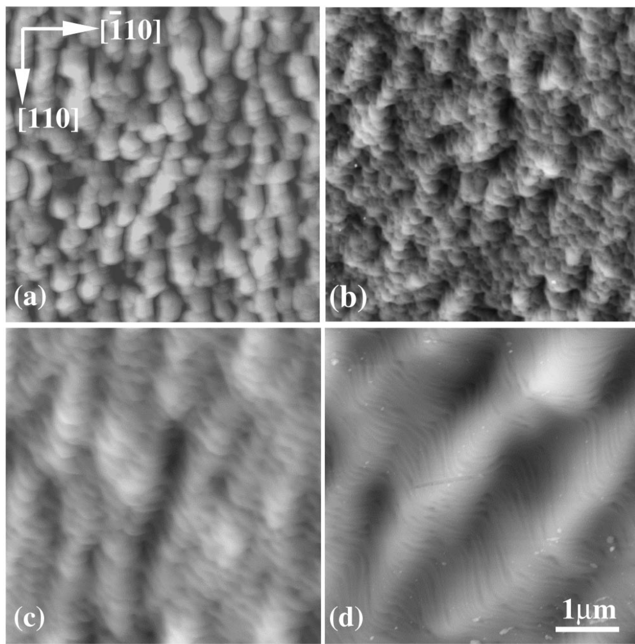

FIG. 1. Atomic-force micrographs of the surfaces of (a) 0.1-μm-, (b) 0.2-μm-, (c) 0.55-μm-, and (d) 1.5-μm-thick InSb films grown on GaAs. The gray-scale ranges displayed are (a) 40 nm, (b) 30 nm, (c) 50 nm, and (d) 100 nm, respectively.

using Cu $K\alpha$ radiation monochromated by a four-reflection Si(220) monochromator. The data were collected at several azimuthal angles to obtain the angle of rotation of the epilayer planes about an in-plane tilt axis (epilayer tilt) and out-of-plane d spacings. An orthorhombic crystal symmetry was assumed in the analysis.

The carrier concentrations and electron mobilities of the films were determined using room-temperature resistivity and Hall measurements, both in the van der Pauw configuration.[32] Depth-dependent carrier concentrations and electron mobilities of 0.55- and 1.5-μm-thick films were also measured with a Bio-Rad Microscience Hall Profiler. Using this instrument, the transport properties were measured, followed by anodization and acid etching of the sample, removing ~12 nm per step. This sequence of measurement and film removal was repeated automatically until the substrate was reached.

III. RESULTS AND DISCUSSION

A. Surface morphology

Figures 1(a)–1(d) show representative AFM images for each of the films. Several parameters determined from analyses of these images, include typical feature heights, root-mean-square surface roughness R_{rms}, and the ratios of R_{rms} to the film thickness t are tabulated in Table I. It is evident in Fig. 1(a) that the 0.1-μm-thick films consists of coalescing islands with a rectangular shape. This is further confirmed by the cross-sectional TEM image displayed in Fig. 2, which shows evidence for coalescing islands. Most of the islands are elongated along the [110] direction, with a width about 500 nm, lengths ranging from 500 to 1250 nm, and heights 10 to 20 nm. For the 0.2 μm films, the island widths are

TABLE I. Feature height, root-mean-square surface roughness R_{rms}, and the ratios of R_{rms} to the film thickness t for the InSb films.

t (μm)	Feature height (nm)	R_{rms} (nm)	R_{rms}/t (%)
0.1	10–20	4.91	4.91
0.2	5–10	1.6	0.98
0.55	10–30	5.37	0.98
1.5	30–60	14.79	0.99

typically ~1000 nm and island length is essentially unchanged. The width, lengths, and heights of the islands of 0.55 μm thick have increased slightly. For the 1.5 μm films, the islands have elongated to nearly 2.5 μm features with 30–60 nm surface undulations. As the film thickness increases, the elongation direction of the islands rotates. For the 0.1 and 0.55 μm films, the islands elongate in nearly [110] direction. However, for 0.2 and 1.5 μm films, the elongation direction deviates from [110] toward the [100] direction.

As listed in Table I, as the film thickness increases from 0.1 to 0.2 μm, the R_{rms} value drops by more than a factor of 2, indicating a much smoother film. When the film thickness increases beyond 0.2 μm, R_{rms} continues increasing in proportion to the film thickness, resulting in a nearly constant R_{rms}/t ratio of approximately 1%. Interestingly, for the 0.1-μm-thick films, the R_{rms}/t ratio is nearly 5%. The differences in the R_{rms}/t ratios between the films apparently correlate with differences in the growth mode. The 0.1 μm films contain islands which are not completely coalesced, such that the film growth is three-dimensional, and the R_{rms}/t ratio is large. On the other hand, for the thicker films, with the smaller R_{rms}/t ratio, the islands are apparently fully coalesced and the films are able to grow two-dimensionally.

In order to quantify the spatial length scales of the surface roughness, we performed both one-dimensional (1D) and two-dimensional power spectral density analyses on the 5×5 μm AFM images shown in Fig. 1. Figures 3(a) and 3(b) display typical one-dimensional PSD analyses, collected in the [$\bar{1}$10] and [110] directions, respectively. Note that for the

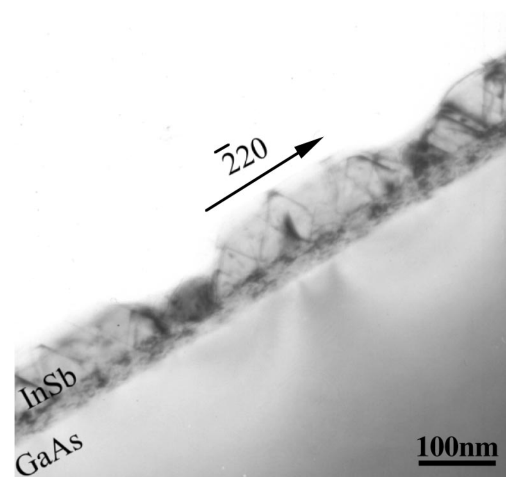

FIG. 2. Bright-field cross-sectional TEM image of the 0.1-μm-thick InSb films under [$\bar{2}$20] two-beam condition.

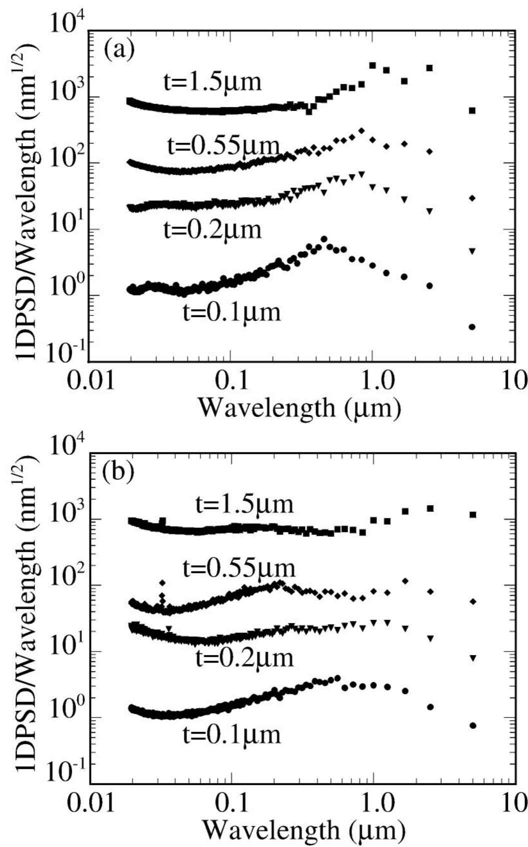

FIG. 3. One-dimensional power spectral density (1DPSD) along the (a) $[\bar{1}10]$ and (b) $[110]$ directions for each of the films.

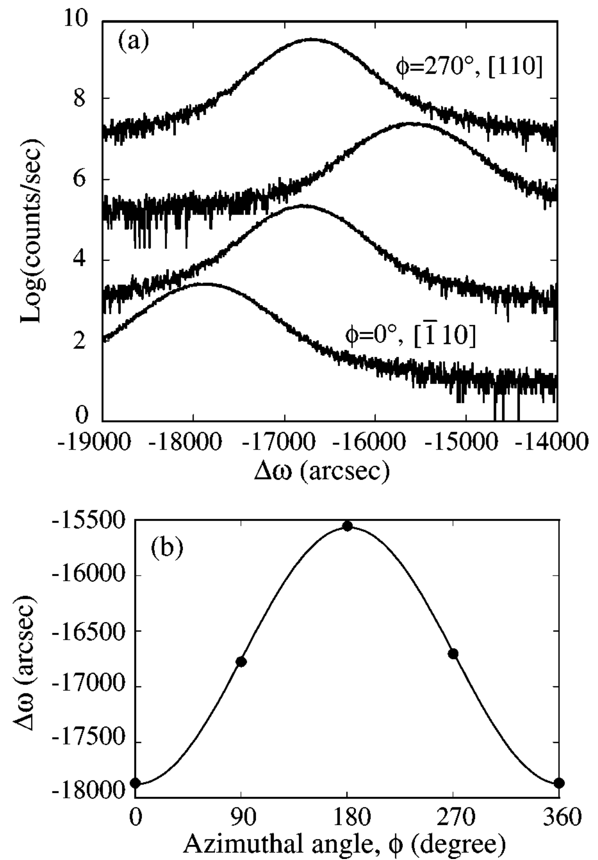

FIG. 4. (a) (004) rocking curves of 0.55 μm InSb film. The data were collected for four azimuthal angles in 90° increments from 0° to 270°; (b) The angular separation between the epilayer and substrate peaks, $\Delta\omega$, as a function of azimuthal angle ϕ. The line represents a sinusoidal fit to the data.

one-dimensional PSD analyses of the 0.55 and 1.5 μm films [Figs. 1(c) and 1(d)], we analyzed additional AFM images which were rotated by 15° and 30°, respectively, such that the surface features were aligned with the edges of the image. The wavelengths at which an apparent peak in the 1D-PSD/wavelength versus wavelength occurs are expected to be correlated with the spatial length scale of a specific surface feature.[21] In the $[\bar{1}10]$ direction, shown in Fig. 3(a), apparent peaks in wavelength occur at approximately 0.5, 0.9, 0.84, and 1 μm for the 0.1, 0.2, 0.55, and 1.5 μm films, respectively. These wavelengths correspond well with the island widths discussed earlier. In addition, for the 0.1 μm film, a lower intensity peak at approximately 25 nm is apparent. The wavelength of this peak is dependent on the image size such that it appears to be an artifact related to either bit noise in the AFM image collection process or edge effects in the PSD analysis. Figure 3(b) presents the 1D-PSD analyses in the $[110]$ direction. In this case, the predominant peaks in the wavelength occur at approximately 0.5, 1.0, 1.68, and 2.46 μm for the 0.1, 0.2, 0.55, and 1.5 μm films, respectively. The significant increase in the wavelengths for the 0.55 and 1.5 μm films corresponds well with the elongation of the features observed in the AFM images in Figs. 1(c) and 1(d). In addition, there are indications of lower-intensity peaks at shorter wavelengths, close to 0.2 μm, for all of the films. In particular, these peaks occur at 0.2, 0.26, 0.22, and 0.15 μm for the 0.1, 0.2, 0.55, and 1.5 μm films, respectively. These shorter-wavelength features correspond to the spacing between bilayer height surface features which are evident in the AFM images in Figs. 1(a)–1(d). Consequently, as we will discuss later in this article, there are no features apparent in either the AFM images or the PSD analyses of the AFM images, which occur at length scales comparable to the Fermi wavelength.

B. Epilayer tilt

In Fig. 4(a), we present a series of rocking curves for the 0.55 μm films, collected at four azimuthal angles in 90° increments from 0° to 270°, corresponding to the $[\bar{1}10]$, $[\bar{1}\bar{1}0]$, $[1\bar{1}0]$, and $[110]$ directions. Similar measurements were performed on the other films. From these rocking curves, we measured the angular separation $\Delta\omega$ between the epilayer and substrate peaks for different azimuthal angles. We then determined the epilayer tilt by plotting $\Delta\omega$ versus azimuthal angle ϕ and fitting the data with a sinusoidal wave, Fig. 4(b). The resulting amplitude and phase of the wave indicate the magnitude and axis of epilayer tilt.[33]

Table II lists the magnitude and axis of epilayer tilt of all of the films. The axis of tilt is indicated by δ, the magnitude of the deviation of the tilt axis from $[010]$ toward $[110]$, as shown in Fig. 5(a). Table II also includes the magnitude of tilt, resolved in the $[\bar{1}10]$ and $[110]$ directions. Positive tilt values indicate tilt of epilayers in the direction opposite to

TABLE II. Variation of epilayer tilt with the film thickness t. δ is the magnitude of the deviation of the tilt axis from [010] toward [110]. For δ=45°, the tilt axis is [110]. The negative tilt magnitude indicates that the epilayer tilts in the same direction as the substrate offcut, thereby increasing the offcut.

t (μm)	Tilt magnitude	δ	Resolved tilt	
			[110]	[$\bar{1}$10]
0.1	0.108°	40.5°	0.022°	0.106°
0.2	0.178°	63.8°	−0.072°	0.127°
0.55	0.314°	41.2°	0.010°	0.322°
1.5	0.119°	59.3°	−0.015	0.115°

that of the substrate offcut, thus reducing the miscut, as shown in Fig. 5(b). On the other hand, negative tilt values indicate the presence of tilt in the *same* direction as the resolved substrate offcut, which *increases* the miscut. For the 0.1 and 0.55 μm films, the tilt axes are close to the [110] direction. On the other hand, for the 0.2 and 1.5 μm films, the tilt axes deviate from [110] toward the [100] direction. It is interesting to note that the islands (shown in the AFM images in Fig. 1) tend to be elongated in nearly the same direction as the epilayer tilt axis. For all of the samples, the resolved tilts are not equal in the [110] and [$\bar{1}$10] directions, indicating that the epilayer tilt is asymmetric about the substrate offcut axis. In the [110] direction, the magnitudes of the resolved tilts are less than 0.08° for all of the films and may be positive or negative, indicating that the [110] tilt may increase or decrease the [110] component of the substrate offcut. In the [$\bar{1}$10] direction, the magnitude of epilayer tilt increases from 0.1 to more than 0.3° as the film thickness increases up to 0.55 μm, indicating that the [$\bar{1}$10] tilt mostly decreases the [$\bar{1}$10] component of the substrate offcut. Surprisingly, for the 1.5 μm film, this trend does not continue, as the [$\bar{1}$10] tilt component is reduced to 0.12°. Both the negative value of the [110] resolved tilt and the decreasing value of the [$\bar{1}$10] resolved tilt for the thickest film suggests the presence of reverse tilt, where the tilt increases the miscut.[34,35]

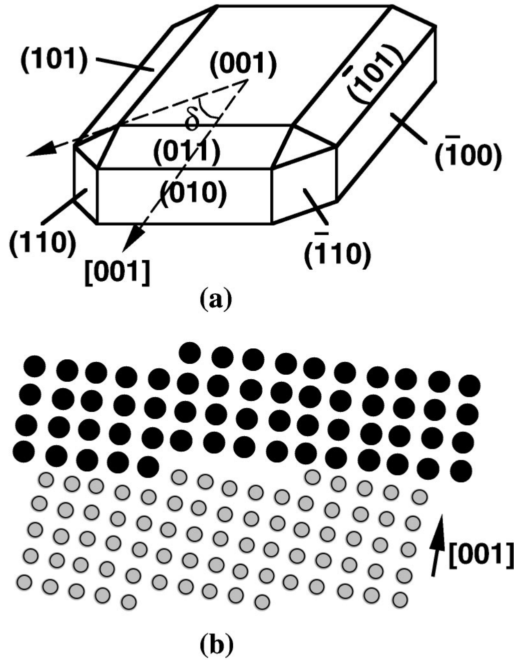

FIG. 5. (a) Crystallographic planes of (001) GaAs. δ is the magnitude of the deviation of the tilt axis from [010] toward [110]. (b) Schematic showing epilayer planes tilting in the direction opposite to that of the substrate miscut.

In lattice-mismatched III–V compounds, plastic relaxation may occur by the generation of 60° $a/2\langle 110\rangle$ {111} misfit dislocations. These dislocations glide to the interface on {111} planes, and the Burgers vector, $a/2\langle 110\rangle$, makes a 60° angle with the $\langle 110\rangle$ line direction. Thus, the dislocations have edge and screw interfacial components, and a tilt component perpendicular to the interface. When the eight possible slip systems are activated equally, the net screw and tilt components are zero, and each system contributes an edge component, $b_{\mathrm{edge}}=a/4[110]$, towards relaxation of the strain. However, in the case of a film grown on a vicinal substrate, the net screw and tilt components will be nonzero, resulting in possible rotation and tilt of the epilayer.[36] The magnitude of the epilayer tilt caused by the tilt component of a 60° misfit dislocation can be calculated using $\tan^{-1}(b/d)$, where $b=a/2$ and d is the average spacing between 60° misfit dislocations. Using cross-sectional HRTEM, we examined the misfit dislocations at the interface between a 0.2 μm InSb film and the GaAs substrate. Over a range of ~142 nm, we find seven $(a/2)[0\bar{1}1]$ 60° misfit dislocations and five $(a/2)[10\bar{1}]$ 60° misfit dislocations. Thus, the net tilt of this 0.2 μm InSb film is ~0.245° in the [$\bar{1}$10] direction. This value is larger than that from HRXRD measurements, 0.127°, as listed in Table II. This apparent inconsistency between HRTEM and HRXRD may be due to the more limited field of view available in HRTEM measurements. Another possible explanation is that the tilt caused by an imbalance in the distribution of 60° dislocations has been partly offset by bilayer height features on the surfaces of our films, as shown in the AFM images in Fig. 1. This is further supported by our observations of reverse tilt discussed earlier. Similarly, in the lower-mismatch $In_xGa_{1-x}As$/GaAs system, reverse tilt was observed, and correlated with the presence of microscale facets.[34] We are currently investigating the origin of both the asymmetric and the reverse tilt through further comparisons of (110) and ($\bar{1}$10) cross-sectional HRTEM analysis with HRXRD and AFM.[37]

C. Strain relaxation

Using (004) HRXRD measurements, we determined the out-of-plane d-spacing d_{001}^{InSb} of the InSb films. Assuming an orthorhombic crystal symmetry and taking the GaAs substrate lattice constant a_{GaAs} as an internal standard, d_{001}^{InSb} was calculated as follows:

$$d_{001}^{\mathrm{InSb}}=\frac{\sin\theta_B}{\sin(\theta_B+\overline{\Delta\omega})}d_{001}^{\mathrm{GaAs}}, \tag{2}$$

where d_{001}^{GaAs} and θ_B are the (001) d spacing and the Bragg angle of the GaAs substrate, respectively, and $\overline{\Delta\omega}$ is the average value of the angular separation between the substrate

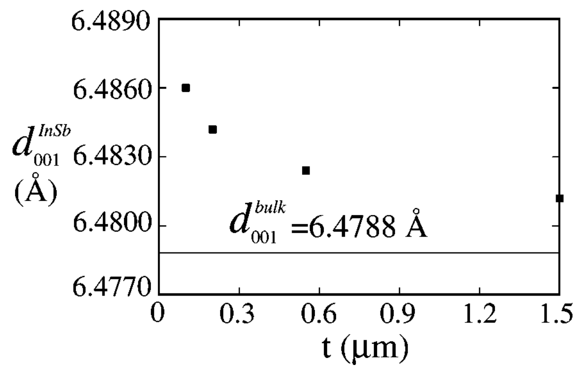

FIG. 6. Variation of out-of-plane d spacing of InSb, d_{001}^{InSb}, with the film thickness t indicating that the residual strain decreases as the film thickness increases.

and film (004) peaks (i.e., the tilt-corrected $\Delta\omega$ value). The calculated d_{001}^{InSb} as a function of thickness is plotted in Fig. 6. It is evident that d_{001}^{InSb} decreases as the film thickness increases, indicating a decreasing residual strain. Since all the film d spacings are within 0.1% of the bulk InSb value, the films are nearly fully relaxed. For each film, we have also calculated the average $\Delta\omega$ resolved in the [110] and $[\bar{1}10]$ directions. Both of them are very close to the average value of $\Delta\omega$, suggesting a symmetric in-plane strain relaxation. We have also performed (115) off-axis measurements in an attempt to determine the in-plane lattice parameters. However, both the small-angle approximation[38] and the tetragonal distortion approximation[39,40] introduce significant errors in the data analysis in this highly mismatched system.

We have also examined misfit dislocations at the epilayer/substrate interface, using high-resolution transmission electron microscopy. In (110) cross sections, we primarily find pure-edge dislocations with the Burgers vector $\mathbf{b} = (a/2)[1\bar{1}0]$, with a few 60° misfit dislocations with $\mathbf{b} = (a/2)[10\bar{1}]$ or $\mathbf{b} = (a/2)[0\bar{1}1]$. For example, in the Fourier-filtered (110) cross-sectional HRTEM image of a 0.2 μm InSb film in Fig. 7, three pure-edge misfit dislocations and one $(a/2)[10\bar{1}]$ 60° misfit dislocation are apparent. Furthermore, most of the misfit dislocations are observed at the InSb/GaAs interface. In addition, a few 60° misfit dislocations are observed in the InSb films, up to 5 nm *away from the interface*. In an earlier report, the latter observation was attributed to the presence of an interlayer at the interface.[19] However, our HRTEM images do not suggest the presence of such an interfacial layer. Instead, the observation of 60° misfit dislocations away from the interface may indicate the movement of misfit dislocations from the surface to the interface. Thus, it is likely that the pure-edge dislocations, and possibly a few of the 60° misfit dislocations, formed during island growth while most of the 60° misfit dislocations formed gradually after continuous coverage was achieved, by moving into the interface from the surface of the epilayer (i.e., by surface nucleation).[41] Hence, as the film thickness increased, additional 60° misfit dislocations would form, resulting in a decreasing residual strain. This trend is consistent with the decrease of residual strain with the film thickness discussed earlier. Interestingly, only pure-edge misfit dislocations have been identified for MBE-grown InSb/GaAs films,[4,6,8] while both pure-edge and a few 60° dislocations were observed in temperature-gradient vapor-transport deposition-grown and MOCVD-grown films.[19,42]

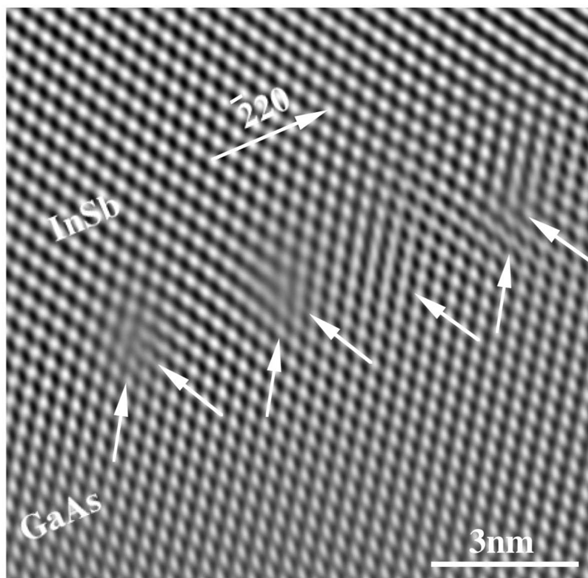

FIG. 7. Fourier-filtered (110) cross-sectional HRTEM image of 0.2-μm-thick InSb film. Both 60° and pure-edge misfit dislocations exist at the InSb/GaAs interface.

We counted the number of each type of misfit dislocations at the interface between the 0.2 μm InSb film and the GaAs substrate. Over a range of ~142 nm along the $[\bar{1}10]$ direction in the (110) cross section, we find 51 pure-edge dislocations, seven $(a/2)[0\bar{1}1]$ 60° misfit dislocations, and five $(a/2)[10\bar{1}]$ 60° misfit dislocations. The strain ϵ relieved by a misfit dislocation can be estimated with the following:

$$\epsilon = b/d, \tag{3}$$

where d is the average dislocation spacing and b is the magnitude of the component of the Burgers vector parallel to the interface. For pure-edge and 60° misfit dislocations, b is equal to $(\sqrt{2}/2)a$ and $(\sqrt{2}/4)a$, respectively. Using the average of the lattice parameters of bulk InSb and GaAs as a, the strains relieved by pure-edge misfit dislocations and 60° misfit dislocations are ~12.4% and 1.8%, respectively. Therefore, for our highly mismatched system, we conclude that the strain in the $[\bar{1}10]$ direction is relieved mainly by pure-edge dislocations. Since our HRXRD measurements have shown that the strain relaxation is symmetric in $\langle 110 \rangle$ in-plane directions, we expect that a similar amount of strain is relaxed in the [110] direction. Furthermore, the effects of substrate misorientation on the shear stresses due to misfit strain on the glide plane in the glide direction were calculated in an earlier study.[34] For our particular miscut, the resolved shear stresses in the [110] and $[\bar{1}10]$ directions are identical.[34] Consequently, classical models for dislocation nucleation and glide based upon resolved shear stress arguments would predict an equal density of pure-edge dislocations in the [110] and $[\bar{1}10]$ directions.[36] Thus, the misfit in our system might be accommodated by a network of equal density

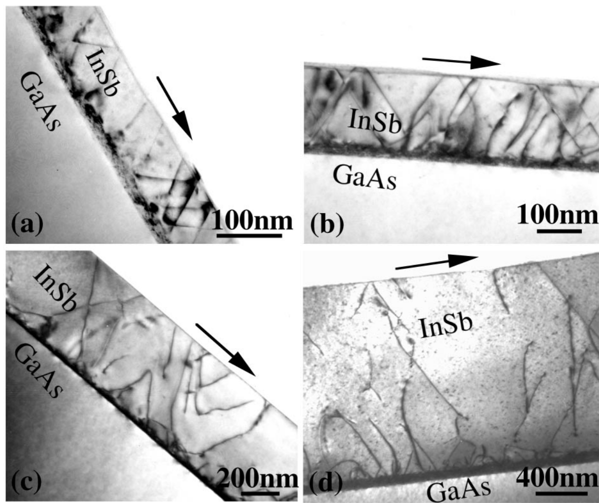

FIG. 8. Bright-field cross-sectional TEM images of InSb films with thicknesses of (a) 0.1 μm, (b) 0.2 μm, (c) 0.55 μm, and (d) 1.5 μm. All the images were collected under a two-beam condition with $\mathbf{g}=[\bar{2}20]$, which is in the direction of the arrow in each image.

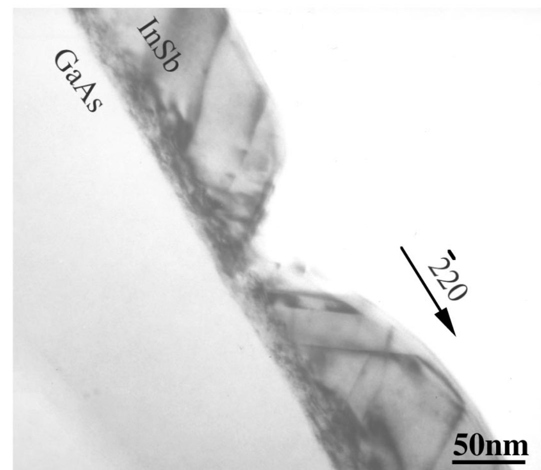

FIG. 9. Bright-field cross-sectional TEM images of 0.1-μm-thick InSb films under $[\bar{2}20]$ two-beam condition. The islands appear to contain threading dislocations at their boundaries.

$(a/2)[110]$ and $(a/2)[1\bar{1}0]$ edge dislocations. On the other hand, in highly mismatched zinc-blende structures, the formation of pure-edge dislocations has been contributed to the interaction of two 60° misfit dislocations during island coalescence.[43] Since island coalescence in our films has occurred *primarily* in the $[\bar{1}10]$ direction, it is likely that much of the strain in the [110] direction is relaxed by 60° misfit dislocations. In that case, an imbalance in the number of 60° misfit dislocations with ''up'' and ''down'' tilt components might occur such that the net tilt is either positive or negative, resulting in either regular or reverse epilayer tilt, respectively. It is interesting to note that in these films, reverse tilt is observed in the [110] direction. Work is underway to examine correlations between the misfit dislocations in both ⟨110⟩ directions and symmetric in-plane strain relaxation and asymmetric and reverse epilayer tilt.[37]

D. Threading dislocations

Figures 8(a)–8(d) show representative cross-sectional TEM images for each of the films. These images reveal that the threading dislocation density decreases monotonically in the growth direction. All the films contain a high density of threading dislocations within ~20 nm of the InSb/GaAs interface. Beyond this region, the dislocation density decreases abruptly, due to several possible mechanisms, including annihilation of dislocations with opposite Burgers vectors and bending of dislocations to form half loops near the interface.[7] In both the 0.55- and 1.5-μm-thick films, the threading dislocation density decreases significantly for film thicknesses beyond 0.3 μm, similar to an earlier study of MBE-grown InSb.[7]

In Fig. 9, we present a bright-field cross-sectional TEM image of a 0.1-μm-thick InSb film, in a region containing coalescing islands. It is apparent that the coalescing islands contain threading dislocations at their boundaries. This suggests that the island boundaries are important sources of threading dislocations in InSb films, as has been reported in Ref. 8.

Figure 10 displays plan-view transmission electron microscopy images of InSb films with thicknesses ranging from 0.1 to 1.5 μm. It is evident from these images that the dislocation density decreases with increasing film thickness. We counted the number of threading dislocations over areas of ~2.58, 2.6, 14.29, and 32.06 μm^2 for the 0.1, 0.2, 0.55, and 1.5 μm films, respectively. We find that the resulting threading dislocation density varies from $\sim 10^{11}\,cm^{-2}$ for the 0.1 μm film to $\sim 4.0\times 10^{8}\,cm^{-2}$ for the 1.5 μm film. Note that the images of the 0.55 and 1.5 μm films, such as those in Figs. 10(c) and 10(d), include only the top ~0.2 μm of the films. Hence, for the 0.55 and 1.5 μm films, the apparent dislocation densities are artificially lower than the actual threading dislocation densities. Furthermore, for the 0.1 μm

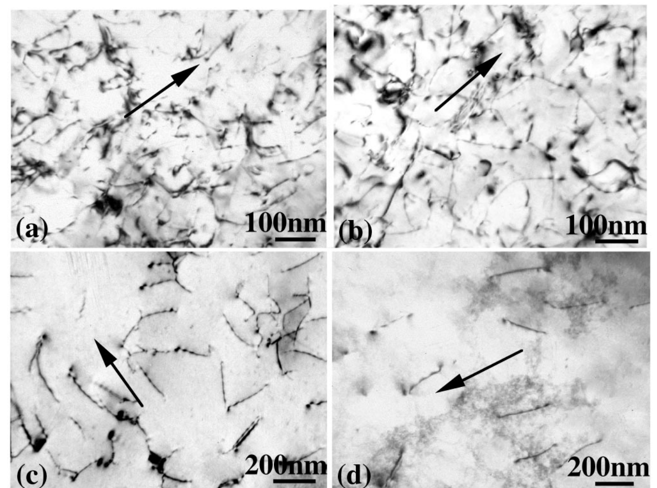

FIG. 10. Plan-view TEM images of (a) 0.1-μm-, (b) 0.2-μm-, (c) 0.55-μm-, and (d) 1.5-μm-thick films. It is evident that the threading dislocation density decreases with increasing film thickness. All the images were collected under a two-beam condition with $\mathbf{g}=[\bar{2}20]$, which is in the direction of the arrow in each image.

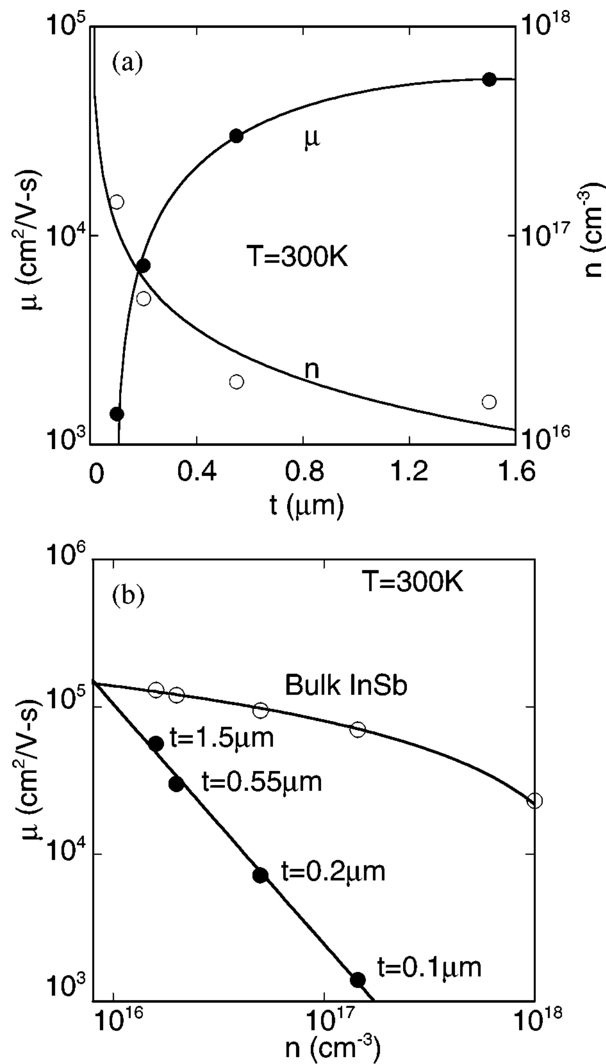

FIG. 11. (a) Variation of the electron mobility μ and the carrier concentration n as a function of film thickness t. (b) A comparison of μ as a function of carrier concentration n of InSb films with those predicted for bulk InSb (see Ref. 44). In both (a) and (b), the error bars are smaller than the size of the data points and the lines are intended as a guide to the eye.

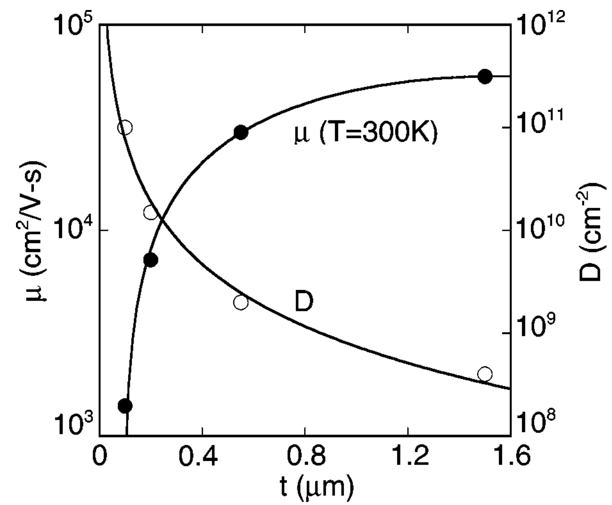

FIG. 12. Film thickness t dependence of the electron mobility μ and dislocation density D. The error bars are smaller than the size of the data points and the lines are intended as a guide to the eye.

film, the high dislocation density may lead to overlapping strain contrast from adjacent dislocations. Therefore, the threading dislocation density of the 0.1 μm film may be underestimated.

E. Electronic properties

Figure 11(a) shows the electron mobility and carrier concentration as a function of film thickness. As the film thickness increases, the carrier concentration decreases and the electron mobility increases. In the thinnest films, a high density of dislocations act as acceptor-like traps, thereby reducing the magnitude of the Hall coefficient $|R_H|$, resulting in an increased carrier concentration and a decreased electron mobility.[2] Figure 11(b) compares the electron mobility as a function of carrier concentration for our InSb films with those predicted for bulk InSb.[44] It is evident that the electron mobilities of our InSb films are much lower than that of bulk InSb. As the film thickness increases, the electron mobilities of the films become comparable to that of bulk InSb. These results suggest that some film thickness-dependent factors are limiting the room-temperature electron mobility of these InSb films.

According to Matthiessen's rule, the total mobility μ of a thin film is related to μ_b and μ^* through

$$1/\mu = 1/\mu_b + 1/\mu^*, \tag{4}$$

where μ_b is the intrinsic electron mobility of the bulk material, and μ^* is the mobility limited by additional scattering mechanisms. These additional scattering mechanisms might be related to structural factors, including residual strain, surface roughness, interface roughness, and threading dislocations. HRXRD results have shown that all of the films are nearly fully relaxed. Therefore, we expect that residual strain is not the prominent mobility-limiting factor for these InSb films. Examination of the InSb/GaAs interface with HRTEM

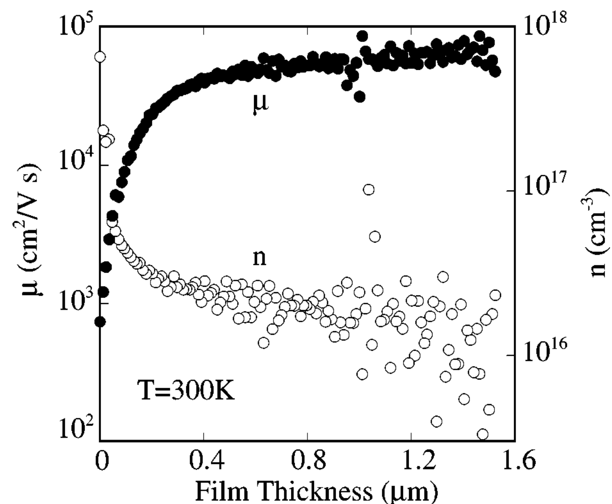

FIG. 13. Depth-dependent electron mobility μ and carrier concentration n of a 1.5-μm-thick film. An abrupt transition in the electron mobility occurs at ~0.3 μm from the InSb/GaAs interface.

showed insignificant interface roughness. Therefore, the interface roughness does not apparently significantly impact the room-temperature electron mobility of these InSb films.

We also considered surface roughness scattering as a possible mobility-limiting mechanism. Surface roughness may reduce the electron mobility when the spatial length scale of the roughness is comparable to the Fermi length λ_F.[21] Treating these bulk-like films as a three-dimensional electron gas, the Fermi wavelength is expressed as $\lambda_F = 2\pi/(3\pi^2 n)^{1/3}$, where n is the free-carrier concentration. Thus, for our 0.1-, 0.2-, 0.55-, and 1.5-μm-thick InSb films, the Fermi wavelengths are 38.7, 55.1, 74.8, and 79.0 nm, respectively. The PSD analyses presented in Fig. 3 showed no evidence of surface features with spatial length scales near these Fermi wavelengths. Furthermore, we have shown in Table I that all the samples have a small rms roughness to film thickness ratio $R_{\rm rms}/t$. Therefore, we expect that the surface roughness has not significantly affected the electron mobility.

Figure 12 shows the film thickness dependence of the electron mobility compared with that of the dislocation density. It is evident that as the film thickness is increased, the electron mobility increases and the dislocation density decreases. In particular, for the 0.1-μm and the 1.5-μm-thick films, the threading dislocation density decreases from 1×10^{11} to $4\times10^{8}/\mathrm{cm}^2$, while the electron mobility increases from $\sim$1400 to $\sim$56 000 $\mathrm{cm}^2/\mathrm{V\,s}$. These data imply that dislocation scattering limits the room-temperature electron mobility of our InSb films.

This assertion is further supported by the depth-dependent electron mobility and carrier concentration of the 1.5-μm-thick films presented in Fig. 13. As the 1.5 μm film is etched away (decreasing film thickness), it is evident that the electron mobility decreases and the carrier concentration increases near the substrate region. The 0.55-μm-thick film exhibits similar depth-dependent electron mobilities and carrier concentrations. Note that this trend is similar to the film thickness dependence of the electron mobility and carrier concentration, as shown in Fig. 11(a). For the highest film thickness (i.e., 0.55 and 1.5 μm), similar carrier concentrations were determined from depth-dependent and thickness-dependent Hall measurements. For the lower film thickness (i.e., 0.1 and 0.2 μm), the depth-dependent carrier concentrations are about 30% smaller than the thickness-dependent carrier concentrations. This may be due in part to discrepancies in the apparent thickness of the film, as it is etched away during the electrochemical Hall measurement. On the other hand, the etching process may increase the defect density, effectively lowering the apparent carrier concentration. In any case, the decrease in electron mobility occurs simultaneously with an increase in threading dislocation density, suggesting that free-carrier scattering from threading dislocations has reduced the electron mobility. Interestingly, for both 1.5 and 0.55 μm films, an abrupt drop in the electron mobility occurs at $\sim$0.3 μm from the InSb/GaAs interface. Furthermore, XTEM has shown that the threading dislocation density is significantly decreased as the film thickness is increased beyond 0.3 μm. These results strongly suggest that the electron mobility is limited by the scattering of free carriers from the threading dislocations.

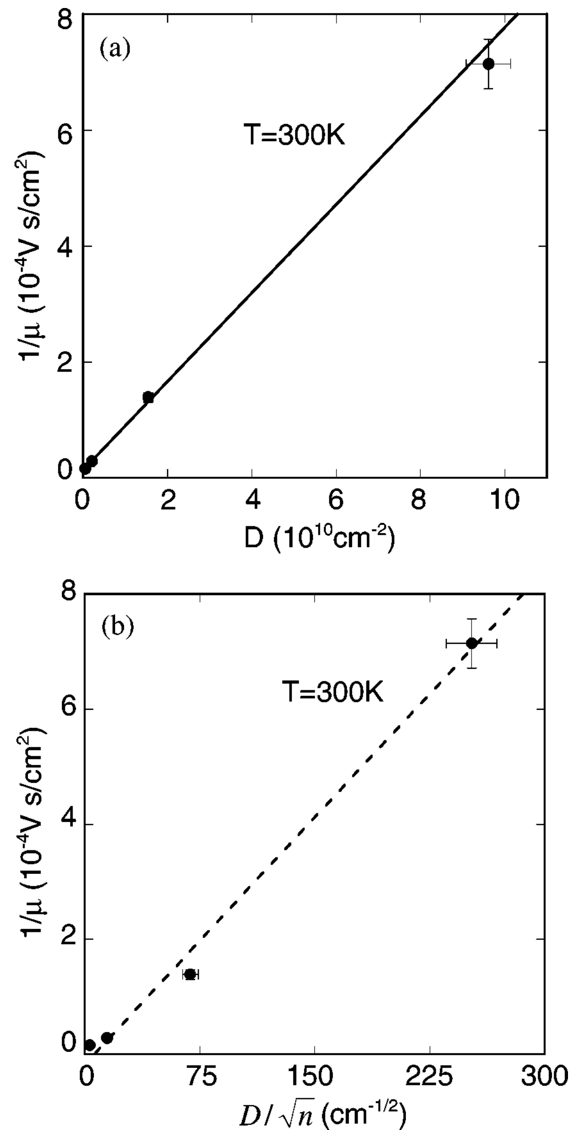

FIG. 14. Variation of the inverse of the electron mobility $1/\mu$ as a function of (a) dislocation density D and (b) $D/\sqrt{n}$, where n is the free-carrier concentration. In (a) and (b), the lines represent (a) weighted least-square and (b) linear least-square fits to the data, respectively. For the left-most two data points of both (a) and (b), the error bars are smaller than the size of the data points.

To investigate the effects of threading dislocations on the electron mobility *quantitatively*, we have considered both the Dexter–Seitz model[27] and the Pödör model.[26] These two models consider free-carrier scattering from the lattice dilation associated with the dislocations (deformation potential scattering) and free-carrier scattering from the depletion potential surrounding the dislocations (Coulomb potential scattering), respectively. For the 0.55- and 1.5-μm-thick films, the dislocation densities were measured for the top $\sim$0.2 μm of each films. Therefore, in these analyses, we use the average electron mobilities of the top 0.208 μm layers of each film. We calculated the mobility of those top 0.208 μm layers, using the following analysis of the depth-dependent Hall data mentioned earlier:[45]

$$R=\frac{t\sum_i R_i\sigma_i^2 t_i}{\sum_i \sigma_i t_i} \tag{5}$$

and

$$\sigma=\frac{\sum_i \sigma_i t_i}{t}, \tag{6}$$

where R, σ, and t are the Hall coefficient, conductivity, and thickness of the entire layered structure, respectively. The quantities with subscripts correspond to the values for each layer.

According to the Dexter–Seitz model,[27] deformation potential scattering associated with edge dislocations results in a mobility limited by dislocations scattering μ_D, which is inversely proportional to the density of edge dislocations D as follows:

$$\frac{1}{\mu_D}=\left[\frac{3\pi}{32}\left(\frac{1-2\nu}{1-\nu}\right)^2\frac{E_1^2\lambda^2 m^*}{k_B T\hbar e}\right]\times D, \tag{7}$$

where E_1 is the hydrostatic deformation potential,[46,47] T is the absolute temperature, k_B is Boltzmann's constant, m^* and e are the effective electron mass and electron charge, λ is the unit crystallographic slip distance, and ν is the Poisson's ratio. Since other structural features, including the residual strain and surface and interface roughness, do not apparently impact the electron mobility of the films, we have assumed that $\mu^*=\mu_D$ and plotted $1/\mu$ as a function of D in Fig. 14(a). Using a weighted least-squares fit of the data,[48] we obtain a bulk mobility value, $\mu_b=(7.86\pm0.60)\times10^4\ \mathrm{cm^2/V\,s}$, which is slightly larger than the reported value, $\mu_b\approx7\times10^4\ \mathrm{cm^2/V\,s}$.[49] The slope of the line, $(7.64\pm0.46)\times10^{-15}\ \mathrm{V\,s}$, is also comparable to $\sim2.20\times10^{-15}\ \mathrm{V\,s}$, the value calculated from Eq. (2) using $E_1=6.53\ \mathrm{eV}$,[47] $\nu=-S_{12}/S_{11}\approx0.335$,[50] and $\lambda=\sqrt{6}a/4\approx3.9674\ \text{Å}$ (where $a=6.4788\ \text{Å}$ is the lattice parameter of InSb).[50] Here, we have used $\lambda=b_e$, the edge components of those dislocations cause the shift of the conduction band, and thus significantly affect the electron mobility.[46,47] These results show a quantitative correlation between increasing dislocation density and decreasing electron mobility, which is consistent with the predictions of the Dexter–Seitz model.

Several studies on n-type GaN films have shown that the Coulomb potential scattering associated with the dislocations is apparently the dominant factor limiting the room-temperature mobility.[51–53] In those cases, the effects of dislocation-induced deformation potential scattering were not considered. Furthermore, in other studies of heavily dislocated n-type GaN, more significant deformation potential scattering than Coulomb potential scattering was reported.[54,55] Here, we have also examined the effect of Coulomb potential scattering on the electron mobility of the InSb films. According to the Pödör model,[26] for a fixed temperature, the electron mobility limited by Coulomb potential scattering μ_C is linearly proportional to $\sqrt{n}/D$. Figure 14(b) shows the measured $1/\mu$ as a function of $D/\sqrt{n}$. Assuming that $\mu^*=\mu_C$, the intercept of a linear least-squares fit to the data yields a negative value for the bulk mobility, indicating that the effect of depletion potential scattering is overestimated in this case. Thus, the electron mobility and free-carrier concentration dependencies on threading dislocation density are not primarily explained by the Pödör model. Therefore, for our unintentionally doped films, the electron mobility is limited mainly by the scattering potential associated with the lattice dilation caused by dislocations, rather than the scattering from a depletion potential surrounding the dislocations. We are currently further investigating the relative roles of depletion potential and lattice dilation scattering on the electron mobility of highly mismatched InSb films, using temperature-dependent Hall and resistivity measurements.

IV. CONCLUSIONS

In summary, we have investigated the evolution of the structure and electronic properties of highly mismatched InSb films, with thicknesses ranging from 0.1 to 1.5 μm. The 0.1-μm-thick films are nearly fully relaxed and consist of partially coalesced islands which appear to contain threading dislocations at their boundaries. When the film thickness is increased beyond 0.2 μm, the residual strain is reduced and the island coalescence is essentially complete. The epilayers have relaxed equally in the $[110]$ and $[\bar{1}10]$ in-plane directions, with both pure-edge and 60° dislocations contributing to the relaxation of strain. Furthermore, epilayer rotation about an in-plane axis (epilayer tilt), which either decreases or increases the substrate offcut, is observed. Interestingly, the coalescing islands discussed above tend to be preferentially aligned along the axis of epilayer tilt. We find that the threading dislocation density decreases with the film thickness, while the corresponding room-temperature electron mobility increases with the film thickness. Other structural features, including residual strain, or surface or interface roughness, do not apparently limit the room-temperature electron mobility of these films. These results suggest that the carrier scattering from threading dislocations is the primary room-temperature electron mobility-limiting mechanism in these films. Finally, we find a *quantitative* correlation between decreasing threading dislocation density and increasing electron mobility, which is consistent with the predictions of the Dexter–Seitz model, while it cannot be explained by the Pödör model. This indicates that the free-carrier scattering from the lattice dilation associated with threading dislocations (deformation potential scattering) rather than scattering from a depletion potential surrounding the dislocations (Coulomb potential scattering) is the dominant factor limiting the room-temperature electron mobility of highly mismatched InSb films.

ACKNOWLEDGMENTS

This work was supported in part by the Offices of the Provost and the Vice President for Research at the University of Michigan, the Dow Corning Foundation, the donors of the Petroleum Research Fund, administered by the American Chemical Society, and the National Science Foundation

(Grant No. DMR-9733707). The authors thank R. Clarke, R. Gibala, and J. Singh for useful comments and E. R. Behringer for assistance with Numerical Recipes in C programing.

[1] J. Heremans, J. Phys. D **26**, 1149 (1993).
[2] M. Yano, T. Takase, and M. Kimata, Phys. Status Solidi A **54**, 707 (1979).
[3] A. J. Noreika, J. Greggi, Jr., W. J. Takei, and M. H. Francombe, J. Vac. Sci. Technol. A **1**, 558 (1983).
[4] G. M. Williams, C. R. Whitehouse, C. F. McConville, A. G. Cullis, T. Ashley, S. J. Courtney, and C. T. Elliot, Appl. Phys. Lett. **53**, 1189 (1988).
[5] J.-I. Chyi, S. Kalem, N. S. Kumar, C. W. Litton, and H. Morkoç, Appl. Phys. Lett. **53**, 1092 (1988).
[6] C. J. Kiely, J.-I. Chyi, A. Rockett, and H. Morkoç, Philos. Mag. A **60**, 321 (1989).
[7] S. D. Parker, R. L. Williams, R. Droopad, R. A. Stradling, K. W. J. Barnham, S. N. Holmes, J. Laverty, C. C. Phillips, E. Skuras, R. Thomas, X. Zhang, A. Staton-Bevan, and D. W. Pashley, Semicond. Sci. Technol. **4**, 663 (1989).
[8] X. Zhang, A. E. Staton-Bevan, and D. W. Pashley, Mater. Sci. Eng., B **7**, 203 (1990).
[9] P. E. Thompson, J. L. Davis, J. Waterman, R. J. Wagner, D. Gammon, D. K. Gaskill, and R. Stahlbush, J. Appl. Phys. **69**, 7166 (1991).
[10] B. R. Bennett, R. Magno, and B. V. Shanabrook, Appl. Phys. Lett. **68**, 505 (1996).
[11] E. Michel, H. Mohseni, J. D. Kim, J. Wojkowski, J. Sandven, J. Xu, M. Razeghi, R. Bredthauer, P. Vu, W. Mitchel, and M. Ahoujja, Appl. Phys. Lett. **71**, 1071 (1997).
[12] J. R. Söderström, M. M. Cumming, J.-Y. Yao, and T. G. Andersson, Semicond. Sci. Technol. **7**, 337 (1992).
[13] R. M. Biefeld and G. A. Hebner, J. Cryst. Growth **109**, 272 (1991).
[14] D. K. Gaskill, G. T. Stauf, and N. Bottka, Appl. Phys. Lett. **58**, 1905 (1991).
[15] Y. Iwamura and N. Watanabe, Jpn. J. Appl. Phys., Part 2 **31**, L68 (1992).
[16] M. Behet, B. Stoll, W. Brysch, and K. Heime, J. Cryst. Growth **124**, 377 (1992).
[17] C. Besikci, Y. H. Choi, R. Sudharsanan, and M. Razeghi, J. Appl. Phys. **73**, 5009 (1993).
[18] D. L. Partin, L. Green, and J. Heremans, J. Electron. Mater. **23**, 75 (1994).
[19] L. H. Kuo, S. Z. Hua, L. Salamanca-Riba, D. L. Partin, L. Green, and J. Heremans, Mater. Res. Soc. Symp. Proc. **340**, 405 (1994).
[20] T. W. Kim, B. S. Yoo, M. A. Mckee, and J. Y. Lee, Phys. Status Solidi A **142**, K23 (1994).
[21] R. M. Feenstra, M. A. Lutz, F. Stern, K. Ismail, P. M. Mooney, F. K. LeGoues, C. Stanis, J. O. Chu, and B. S. Meyerson, J. Vac. Sci. Technol. B **13**, 1608 (1995).
[22] X. Zhang, A. E. Staton-Bevan, D. W. Pashley, S. D. Parker, R. Droopad, R. L. Williams, and R. C. Newman, J. Appl. Phys. **67**, 800 (1990).
[23] G. L. Pearson, W. T. Read, and F. J. Morin, Phys. Rev. **93**, 666 (1954).
[24] W. T. Read, Philos. Mag. **45**, 775 (1954).
[25] W. T. Read, Philos. Mag. **46**, 111 (1955).
[26] B. Pödör, Phys. Status Solidi **16**, K167 (1966).
[27] D. L. Dexter and F. Seitz, Phys. Rev. **86**, 964 (1952).
[28] H. Booyens, J. S. Vermaak, and G. R. Proto, J. Appl. Phys. **48**, 3008 (1977).
[29] H. H. Wieder, Solid-State Electron. **9**, 373 (1966).
[30] T. Takebe, T. Yamamoto, M. Fujii, and K. Kobayashi, J. Electrochem. Soc. **140**, 1169 (1993).
[31] J. M. Elson and J. M. Bennett, Appl. Opt. **34**, 201 (1995).
[32] L. J. van der Pauw, Philips Res. Rep. **13**, 1 (1958).
[33] S. K. Ghandhi and J. E. Ayers, Appl. Phys. Lett. **53**, 1204 (1988).
[34] see, for example, R. S. Goldman, K. L. Kavanagh, H. H. Wieder, S. N. Ehrlich, and R. M. Feenstra, J. Appl. Phys. **83**, 5137 (1998), and references therein.
[35] R. S. Goldman, H. H. Wieder, and K. L. Kavanagh, Appl. Phys. Lett. **67**, 344 (1995).
[36] J. E. Ayers, S. K. Ghandhi, and L. J. Schowalter, J. Cryst. Growth **113**, 430 (1991).
[37] X. Weng, R. S. Goldman, D. L. Partin, and J. P. Heremans (unpublished).
[38] C. R. Wie and H. M. Kim, Proc. SPIE **877**, 41 (1988).
[39] A. T. Macrander, G. P. Schwartz, and G. J. Gualtieri, J. Appl. Phys. **64**, 6733 (1988).
[40] A. Leiberich and J. Levkoff, J. Vac. Sci. Technol. B **8**, 422 (1990).
[41] D. W. Pashley, Adv. Phys. **14**, 327 (1965).
[42] T. W. Kim, H. C. Bae, and H. L. Park, Appl. Phys. Lett. **74**, 380 (1999).
[43] E. P. Kvam, D. M. Maher, and C. J. Humphreys, J. Mater. Res. **5**, 1900 (1990).
[44] V. W. L. Chin, R. J. Egan, and T. L. Tansley, J. Appl. Phys. **69**, 3571 (1991).
[45] R. L. Petritz, Phys. Rev. **110**, 1254 (1958).
[46] J. Bardeen and W. Shockley, Phys. Rev. **80**, 72 (1950).
[47] C. G. Van de Walle, Phys. Rev. B **39**, 1871 (1989).
[48] W. H. Press, S. A. Teukolsky, W. T. Vetterling, and B. P. Flannery, *Numerical Recipes in C*, 2nd ed. (Cambridge University Press, New York, 1996), p. 666.
[49] O. Madelung, *Semiconductors—Basic Data*, 2nd rev. ed. (Springer, Berlin, 1996), p. 146.
[50] M. Neuberger, *Handbook of Electronic Materials* (IFI/Plenum, New York, 1971), Vol. 2, p. 79.
[51] N. G. Weimann, L. F. Eastman, D. Doppalapudi, H. M. Ng, and T. D. Moustakas, J. Appl. Phys. **83**, 3656 (1998).
[52] H. M. Ng, D. Doppalapudi, T. D. Moustakas, N. G. Weimann, and L. F. Eastman, Appl. Phys. Lett. **73**, 821 (1998).
[53] D. C. Look and J. R. Sizelove, Phys. Rev. Lett. **82**, 1237 (1999).
[54] J.-L. Farvacque, Z. Bougrioua, I. Moerman, G. Van Tendeloo, and O. Lebedev, Physica B **273-274**, 140 (1999).
[55] Z. Bougrioua, J.-L. Farvacque, I. Moerman, P. Demeester, J. J. Harris, K. Lee, G. Van Tendeloo, O. Lebedev, and E. J. Thrush, Phys. Status Solidi B **216**, 571 (1999).